Investigation on the Influence of the Arc Region on Heat and Mass Transport in an EAF Freeboard using Numerical Modeling

authored by J. C. Gruber, T. Echterhof, H. Pfeifer

and published in *steel research international*

Contact

Department for Industrial Furnaces and Heat Engineering
RWTH Aachen University
Kopernikusstr. 10
52074 Aachen, Germany

Website: www.iob.rwth-aachen.de/en/
E-mail: contact@iob.rwth-aachen.de
Phone: +49 241 80 25936
Fax: +49 241 80 22289

Investigation on the Influence of the Arc Region on Heat and Mass Transport in an EAF Freeboard using numerical Modeling

Dipl.-Ing. Jacqueline Christina Gruber [1)*], Dr.-Ing. Thomas Echterhof [2)] and Prof. Dr.-Ing. Herbert Pfeifer [3)]

1) Research Assistant at the Department of Industrial Furnaces and Heat Engineering, RWTH Aachen University, Kopernikusstrasse 10, 52074 Aachen, Germany. (Email-Address: gruber@iob.rwth-aachen.de)

2) Senior Engineer and Group Manager Energy and Mass Balances at the Department of Industrial Furnaces and Heat Engineering, RWTH Aachen University, Kopernikusstrasse 10, 52074 Aachen, Germany. (Email-Address: echterhof@iob.rwth-aachen.de)

3) University Professor and Head of the Department of Industrial Furnaces and Heat Engineering, RWTH Aachen University, Kopernikusstrasse 10, 52074 Aachen, Germany. (Email-Address: pfeifer@iob.rwth-aachen.de)

Abstract:

The melting of scrap in an electric arc furnace is a highly energy intensive process, whereby the energy required depends on the individual operational parameters of a heat, size of the furnace and type of steel being produced. In current EAF operation up to and sometimes more than 40 % of the total energy consumption are provided by chemical sources like natural gas, charged and injected carbon etc. Since the optimization of electrical and chemical energy use within the furnace is an important and ongoing process, to use as much of the chemical energy inside the furnace as possible is mandatory. However the high temperatures and electromagnetic interference during the power-on phase make it hard to monitor and control the transient processes within an electric arc furnace. To increase the understanding of heat and mass transfer inside the electric arc furnace freeboard, which directly influences the post-combustion of e.g. CO and H_2, the influence of the arc jets on fluid flow and temperature distribution in the arc region has been investigated using numerical modeling. In this paper we show the results achieved so far and present the conclusions gained as well as the challenges that still have to be overcome.

Keywords: Electric arc furnace, CFD, numerical simulation, heat and mass transfer, furnace freeboard

1. Introduction

To optimize the use of chemical energy in the electric arc furnace (EAF) process it is necessary to understand the interrelationships between the fluid flow field, energy flows and chemical reactions within an EAF freeboard. Due to the harsh conditions inside the EAF freeboard, to monitor or measure these interrelations is extremely difficult up to impossible. Therefore numerical modeling in the form of computational fluid dynamics (CFD) simulation models can give significant insights to optimize e.g. the post combustion inside the EAF vessel.

The importance of post combustion can be seen by the following investigations. Kirschen et al. [1] performed off-gas measurements at two different alternating current (AC) electric arc furnaces (EAF's) for austenitic steel grade heats. Both EAF's considered have a steam cooled shell in order to optimize energy recovery, whereby one of them has a steam cooled roof. The averaged energy balances for the two EAF's show that the loss of sensible and latent heat, due to CO and H_2 in the hot off-gas flowing out of the furnace vessel, makes up between 11 % (steam cooled roof and shell) and 16 % (water cooled roof and steam cooled shell) of the total energy input during one heat. In comparison, the simulation results of a mathematical model developed by Logar et al. [2] for an AC EAF with a conventionally water cooled furnace shell predicts that the flow of off-gas represents 16 % of the total energy input and the cooling approximately 15 %. One way to improve the energy efficiency of a furnace is therefore to reduce the off-gas and cooling losses by increasing the percentage of total input energy transferred to the steel. This can be achieved by for example increasing the degree of combustion of CO and H_2 in the off-gas while they are still inside the vessel.

At present there are only a few examples of CFD models that investigate the processes within an EAF freeboard. Guo et al. [3] present a radiation model to quantify the radiation energy distribution inside an AC EAF during the power-on phase. The radiating surface of the arcs is represented by the extended surface of the cylindrical electrodes, deflected outwards from the furnace center. It is assumed that 80 % of the energy released from an arc is transferred in the form of thermal radiation, with 2 % absorbed by the electrode and 18 % directly transferred to the bath. Using the surface of the cylinders representing the arcs and the active power input rate, the energy flux from the surfaces representing the arcs is calculated and applied as a boundary condition. The temperature distribution resulting from the modeled thermal radiation exchange is presented. The influence of the furnace atmosphere is not considered.

In addition, in order to check the assumption that 2% of the electric energy is absorbed by the electrodes, Guo et al. [3] calculate the electrode temperature distribution resulting from Joule heating due to the current of 61.5 kA and thermal conduction. A temperature of 400 K at the top of the electrode, a hot tip temperature between 2000 K and 3600 K and a uniform furnace atmosphere temperature of 400 K is assumed. It is concluded that no more than 5.5 % of the total electric energy flows into the electrodes at the tip. This calculation does however not consider the thermal radiation absorbed by the electrodes from other surfaces, for example the impingement area of the arc with the bath or the foamy slag surface.

Li et al. [4] developed a 3D simulation model for flat-bath conditions inside an AC EAF freeboard. The aim of the model is to gain insights into the post-combustion using oxygen injectors. A comparison of the post combustion with and without air ingress from the slag door led to the conclusion that air ingress has a detrimental effect on the post-combustion. However, the simplified geometry and boundary conditions, for example the definition of fixed temperatures at the inner surfaces, limit the comparability of the results with a real EAF process. Furthermore the arc region is not included in the model.

The 3D model of the AC EAF freeboard for flat-bath conditions presented by Chan et al. [5] includes the fluid flow, combustion reactions, radiative heat transfer, turbulence and NO_x

formation. The primary objective of the simulations is to identify the main mechanisms of NO_x formation and analyze potential NO_x control strategies when burners and Co-Jets are in operation. The numerical mesh, which has only 82 000 cells, is fairly coarse. The influence of the arc region is not considered.

Henning et al. [6-7] presented a model for a DC Arc furnace that includes not only the fluid flow in the freeboard, but also the fluid flow in the slag and metal bath. The solution domain represents a 5-degree axisymmetric slice of the furnace. The fields of electrical potential, current and magnetism in the electric arc region, as well as convective heat transfer and radiation are taken into account. The metallurgical processes within the bath are included using an energy absorption model. This is the only EAF furnace model that attempts to show the interaction between all fluid zones simultaneously. The gas inside the freeboard is considered to be air. Air ingress, off-gas extraction and the chemical reactions within the freeboard are not considered.

Al-Harbi et al. [8] developed a 3D CFD numerical simulation model for an AC EAF to investigate causes of low service life of the refractory materials in the roof during supersonic oxygen injection. One of the advantages of the model is the concept used to represent the CO source at the slag layer due to decarburization of the melt. It results in a more realistic inhomogeneous source of CO at the slag surface. As the inside of the electrodes and electric arc region are not included in the solution domain, the thermal loading of the roof delta due to the reflected radiation from the electric arcs and the effect of the arc region on the flow field are not considered.

Sanchez et al. [9] presented a model that shows the influence of the foamy slag height on the hot spot formation on the water cooled panels of an AC EAF. A Channel Arc Model (CAM) [10] is used to calculate the energy input from the electric arcs. The AC arcs are represented by three cylinders from the tip of the electrodes to the steel bath. A constant heat flux is defined at the relevant inner surfaces of the furnace freeboard and a constant temperature profile is defined at the surface of the electrodes. The geometry of the model is not adapted in order to simulate the effect of a variation in the slag layer height. Instead the defined energy input of the arcs in MW/arc is varied. The solution domain does not include the inside of the electrodes and does not extend below the liquid slag surface.

In Pfeifer et al. [11] a previous version of the model described in this paper was presented. The main aim of the simulations was to identify the main sources of NO_x formation and to investigate the influence of a variation in the amount of air ingress. The model includes a simulation of the fluid flow, thermal radiation, mass and heat transfer within the EAF freeboard. The oxidation/dissociation of CO/CO_2 as well as the formation of NO_x according to the extended Zeldovich thermal NO mechanism is calculated. The electric arcs are represented by three cylinders which extend to the bath surface. Part of the bath and the foamy slag layer are modeled as solids. The height of the foamy slag layer is equal to two thirds of the arc length.

Summarizing the current state of research, the following can be stated:

(i) The models described above all include the electrode surfaces mostly with a static surface temperature or surface temperature distribution. However, the electrodes themselves are not included in any of the solution domains of the EAF models.

ii) Due to the extreme thermal conditions within the furnace, the only possibility to validate the chemical reaction scheme used, is to compare the simulation results with measurements done in the gap between the elbow and the exhaust duct, for example as described by Kirschen et al. [1] or Pfeifer et al. [11]. Yet only the model of Pfeifer et al. includes the elbow and primary dedusting system including the post-combustion gap.

(iii) Only three of the models include the arc region and only one includes the effect of the momentum of the electric arcs on the flow field.

It is the believe of the authors that to increase the understanding of heat and mass transfer inside the electric arc furnace freeboard, a more complete model combining aspects already dealt with in the state of research had to be developed. The previous model [11] needed to be augmented in such a way, that the thermal radiation, heating of the furnace atmosphere drawn into the arcs as well as the direct energy flows between electrodes, arcs and melt can be qualitatively simulated. Apart from the main objective, to simulate the influence of the electric arc region on the flow field within the furnace freeboard, the electrodes as well as the off gas elbow and primary dedusting system including the post-combustion gap have therefore been included in the solution domain of the numerical model. This is crucial to successfully set up an energy balance for the EAF freeboard with the long term goal of enabling a comparison between the calculated energy flows and the electrical power input.

2. Description of the numerical model

In order to investigate the influence of the arc region on the flow field an arc model is required. Additionally to simulate the heat and mass transfer inside the electric arc furnace freeboard this arc model has to be combined with an electrode and a radiation model.

2.1 Arc model

In reality, fluid from around each plasma arc is drawn into the plasma column, moves along as part of the plasma jet and exits it again. In the case of alternating current (AC) arcs, the plasma jet changes direction as a function of the AC frequency of 50 Hz. In a first step towards including the influence of the flow into and out of the plasma region on the flow field within the freeboard, the three AC arcs as well as the impingement zone of the arcs through the slag to the metal bath are modeled based on the channel arc model (CAM) [12]. The plasma arcs are not part of the solution domain. Instead they are represented as cylindrical surfaces extending from the electrode tip to the bath surface. The radius of the cylindrical surfaces representing the arcs was calculated using the channel arc model (CAM) using equation 1.

$$j_{arc,CAM} = \frac{I_{elec}}{\pi\, r_{arc}^2} \tag{1}$$

For the model a mean electric arc current density ($j_{arc,CAM}$) of 1 kA/cm^2 was used [13]. For an arc current of 63 kA an arc radius of 45 mm results from the arc model.

The mass flow rate being drawn into each arc was approximated using equations 2 and 3[12].

$$\dot{m}_{arc,CAM} = K\, r_{arc}^2\, \rho_{arc}^{0.5}\, I_{elec}^{0.5} \tag{2}$$

$$K = \left(\frac{1}{8}\,\pi\,\mu_0\, j_{arc,CAM,cathode}\right)^{0.5} \tag{3}$$

This corresponds to the mass flow rate through a stationary electric arc according to the CAM. The magnetic field constant (μ_o) is equal to 1.256637 × 10^{-6} (kg m)/(A^2 s^2) and an electric arc current density at the cathode ($j_{arc,CAM,cathode}$) of 4.40 kA/cm^2 is used. The gas density is approximated using the ideal gas equation and was calculated for an average arc temperature of 10000 K at the top of the arc column. A value for the mass flow rate of 0.44 kg/s is obtained.

In contrast to detailed models of DC arcs for example by Quian et al. [14], this model is meant to be a time-averaged representation of the energy input from the arcs into the freeboard. It is as yet a very rough approximation of the real situation, as it does for example not include the change in direction of the plasma jets. The model does however include the energy input due to the heating of the entrained fluid by the arcs. Furthermore, the results make it possible to gain an impression of the influence of the arc region on the flow field in the EAF freeboard.

2.2 Electrode model

In contrast to the models mentioned in the introduction, the electrodes are part of the solution domain. Based on the method used by Guo et al. [3] to investigate the amount of energy absorbed by the electrodes from the arcs, equation 4 is used to calculate the necessary heat source per electrode volume. An electrical specific resistance of the electrodes of 5.2 (Ohm*mm^2)/m, a thermal conductivity of 240 W/(m K) and furthermore the same temperature of 400 K [3] at the top cross-sectional area at the electrode gaps are assumed.

$$\dot{q}''' = \frac{I_{elec}^2 R_{elec}}{V_{electrode}} \quad (4)$$

This way the Joule heat caused by an electric current of 63 kA flowing through the graphite electrodes is taken into account by the definition of a heat source of 343 kW/m^3 in the electrodes. The final temperature profiles on the electrodes result in dependence of the simulated convection and thermal radiation exchange within the freeboard.

2.3 Radiation model

To model the radiation the CFD code ANSYS FLUENT (Version 14.5) was used. From the radiation models included in the code the discrete ordinates model [15,16] was chosen to model the thermal radiation. This model was chosen as not only the radiation exchange between the surfaces, but also the gas radiation can be taken into account. With this model a broad range of optical thicknesses can be analyzed, emissivity and dispersion is taken into account and localized sources of heating are not a problem [9].

Due to the complexity of the phenomena taking place within an EAF vessel, it is necessary to make a number of assumptions and simplifications when attempting to model the heat and mass transfer. Therefore only O_2, CO_2, CO, H_2O, N_2 are considered as gas phase species and only the post-combustion of CO to CO_2 and the dissociation of CO_2 to CO are modeled. Also a complete conversion of injected O_2 to CO and a uniform distribution of this CO source over the complete slag surface are assumed simplifying. Slag phase and part of the metal phase are included in the computational domain but only insofar as to include heat transfer by conduction to achieve a more realistic temperature distribution on the upper surface of the slag, which is also assumed to be flat. The slag and metal phase are therefore in this stage of the model only included as solids.

To additionally reduce complexity and to be able to concentrate on modeling of the arc region as well as the heat and mass transport in the furnace freeboard, it was decided to model the flat-bath refining stage in steady-state.

2.4 Governing equations

The simulated flow field and heat transfer are determined by solving the mass conservation, momentum conservation and energy transport equations. For a steady state simulation using the incompressible ideal gas law for density, the mass conservation equation is given by equation 5, whereby the term S_m represents mass sources defined within the solution domain [15].

$$\nabla \cdot (\rho \vec{v}) = S_m \quad (5)$$

Using the incompressible ideal gas law is permissible, as the static pressure difference between the inflow and the outflow of the vessel is less than 500 Pa for the boundary conditions considered. The local mass fractions (Y_i) of the furnace atmosphere species O_2, CO_2, CO, H_2O, N_2 are calculated using equation 6 for each species i [15].

$$\nabla \cdot (\rho \vec{v}\, Y_i) = -\nabla \cdot \vec{J}_i + R_i + S_i \quad (6)$$

In this equation $\vec{J}_i$ is the diffusion flux of each species i due to gradients of concentration and temperature. R_i is the net rate of production of each species i by chemical reaction. S_i is the rate of creation due to sources, such as the volumetric CO source above the slag layer.

The momentum conservation equation is given by equation 7. The term $\vec{F}$ includes momentum sources due to the mass sources defined within the flow field [15].

$$\nabla \cdot (\rho \vec{v} \vec{v}) = -\nabla p + \nabla \cdot (\bar{\bar{\tau}}) + \rho \vec{g} + \vec{F} \quad (7)$$

The energy transport equation used is equation 8, with the term S_h representing energy sources within the flow field [15], such as the heat of reaction due to post-combustion.

$$\nabla \cdot \left(\vec{v}(\rho E + p)\right) = \nabla \cdot \left[k_{eff} \nabla T - \sum_j h_j \vec{J}_j + \left(\overline{\overline{\tau}_{eff}} \cdot \vec{v}\right)\right] + S_h \tag{8}$$

The radiative heat transfer equation (RTE), equation 9, is solved for an absorbing medium for a finite number of discrete solid angles, each associated with a vector direction $\vec{s}$ [15]. Each octant of the angular space at any spatial location is discretized into N_θ multiplied by N_ϕ solid angles, called control angles. This results in 8 times N_θ times N_ϕ vector directions [15]. For the results presented in this paper an angular discretization of $N_\theta = 3$ and $N_\phi = 4$ was used in order to ensure a sufficient resolution of the thermal radiation. The composition dependent absorption coefficient (a) of the gas within the vessel is calculated using the weighted-sum-of-grey-gases-model, which is described by Smith et al. [17]. For the results presented in this paper the refractive index n of the gas mixture is defined to be equal to 1 and the scattering coefficient σ_s is set to zero.

$$\frac{dI_{rad}(\vec{r},\vec{s})}{ds} + (a + \sigma_s)\, I_{rad}(\vec{r},\vec{s}) = an^2 \frac{\sigma \times T^4}{\pi} + \frac{\sigma_s}{4\pi} \int_0^{4\pi} I_{rad}(\vec{r},\vec{s}')\ \Phi(\vec{s},\vec{s}')\, d\Omega' \tag{9}$$

In order to calculate the turbulent kinetic energy (k), dissipation rate (ε) and turbulent viscosity (μ_t), the realizable k-ε turbulence model [18] with standard wall-functions for the near-wall treatment [19] was chosen. This choice is mainly based on the fact that this combination of turbulence model and wall-functions lead to a good convergence of the simulated heat of reaction. Using the realizable k-ε model means that two additional transport equations (10) and (11) are solved. The first transport equation is for the turbulent kinetic energy k and the second is for the turbulent dissipation rate ε [15].

$$\frac{\partial}{\partial t}(\rho\, k) + \frac{\partial}{\partial x_j}(\rho\, k\, u_j) = \frac{\partial}{\partial x_j}\left[\left(\mu + \frac{\mu_t}{\sigma_k}\right)\frac{\partial k}{\partial x_j}\right] + G_k + G_b - \rho\, \varepsilon - Y_M + S_k \tag{10}$$

$$\frac{\partial}{\partial t}(\rho\, \varepsilon) + \frac{\partial}{\partial x_j}(\rho\, \varepsilon\, u_j) = \frac{\partial}{\partial x_j}\left[\left(\mu + \frac{\mu_t}{\sigma_\epsilon}\right)\frac{\partial \varepsilon}{\partial x_j}\right] + \rho\, C_1\, S_\varepsilon - \rho\, C_2 \frac{\varepsilon^2}{k + \sqrt{\upsilon\, \varepsilon}} + C_{1\varepsilon} \frac{\varepsilon}{k}\, C_{3\varepsilon}\, G_b + S_\varepsilon \tag{11}$$

Whereby

G_k Generation of k due to mean velocity gradients

G_b Generation of k due to buoyancy

Y_M Contribution of fluctuating dilation in compressible turbulence to overall dissipation rate

σ_k, σ_ε Turbulent Prandtl numbers

S_k, S_ε User defined source terms

$C_{1\varepsilon}$=1.44 , C_2=1.9, σ_k=1.0 and σ_ε=1.2.

The post-combustion of CO to CO_2 and the dissociation of CO_2 to CO are modeled using the finite rate / eddy dissipation volumetric reaction option. This means that the rates of the reactions are calculated according to the Arrhenius expressions as shown by equation 12 and 13 and in dependence of the turbulent mixing according to the eddy dissipation model. The smaller of the two values is used. The term $k_{f,r}$ is the forward rate constant for reaction r and $\hat{R}_{i,r}$ is the molar rate of creation or destruction of species i.

$$k_{f,r} = A_r T^{\beta_r} e^{\frac{-E_r}{RT}} \tag{12}$$

$$\hat{R}_{i,r} = 1 \cdot \left(k_{f,r} \prod_{j=1}^{N} [C_{j,r}]^{\left(\eta'_{j,r}+\eta''_{j,r}\right)} \right) \tag{13}$$

3. Model implementation

Regarding geometry and operational conditions the numerical model and its boundary conditions are based on an exemplary industrial AC EAF with a tap weight of 100 tons and an inner vessel diameter of 6.1 m.

3.1 Geometry

The EAF model geometry is shown in **Figure 1**. Contrary to the EAF models described in the previous section, the graphite electrodes, the arc region and the post-combustion gap are all part of the solution domain. Burners, lances or injectors are not included in order to reduce the necessary mesh size. The main dimensions of the geometry are given in **Table 1**.

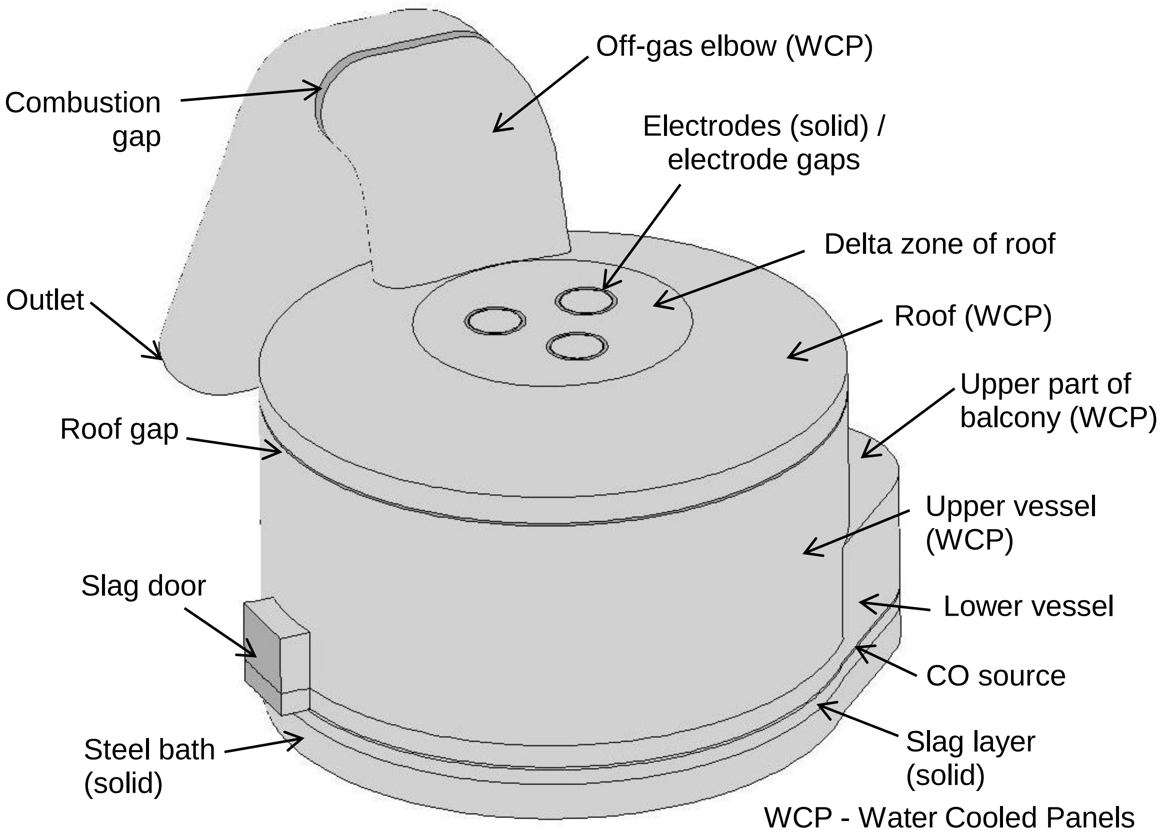

Figure 1: EAF model

Table 1: Main dimensions of the EAF Model

Geometry of EAF Model	
Vessel diameter	6.100 m
Height of vessel from surface of bath to top of roof	3.824 m
Height of slag door	0.650 m
Width of slag door	0.900 m
Area of 4th-hole	2.090 m^2
Size of electrode gaps	0.040 m
Size of roof gap	0.030 m
Height of steel bath layer (solid)	0.400 m
Vertical distance from top of steel bath to bottom of slag door	0.200 m
Height of slag layer (solid)	0.170 m
Height of slag CO source layer	0.030 m
Diameter of electrodes	0.559 m
Electric arc length	0.400 m
Electric arc radius	0.045 m
Arc region: length of negative velocity inlet and mass flow inlet	0.050 m

3.2 Boundary conditions

i) All water cooled surfaces (upper vessel, roof, off-gas elbow, exhaust duct), the lower vessel and delta zone of roof: The walls of the upper vessel of the modeled EAF are cooled by cooling panels. In general the thermal loading of individual panels depends on their position with respect to the slag line, burners and injectors. Therefore the design of the panels differs. The walls of the lower vessel are usually made up of fire bricks and other refractory materials. The inner surface of both the upper and lower vessel in the freeboard is mostly coated with a layer of slag, whose composition, thickness and roughness is not homogeneous and changes continuously during a heat as new material solidifies on the surface or melts, depending on the conditions and thermal loading. For this EAF simulation the upper vessel, off-gas elbow and roof inner surfaces are represented as simple walls (Figure 1) and assumed to be covered by a 20 mm layer of solidified slag. The inner surfaces of the exhaust duct are assumed to be walls covered by a 20 mm layer of dust. The thermal conductivity of both dust and slag layer is defined to be 2.2 W/(m K). The surfaces in contact with the furnace atmosphere are non-slip walls with a roughness height of 5 mm. An emissivity at the inner surfaces of 0.6 is defined. For the upper vessel it is assumed that due to the cooling panels there is a constant temperature of 333 K at the cold outer surface of the slag and dust layer to enable the simulation of thermal conduction through the walls. The inner surfaces of the lower vessel are simplified to be simple walls made of refractory material with a thickness of 500 mm and a thermal conductivity of 2.4 W/(m K). It is assumed that the outside surface of the lower vessel is cooled by natural convection and radiation to the ambient air, which is assumed to have a temperature of 298.15 K. On the outside surface a convection coefficient of 5 W/m^2 K and an emissivity of 0.85 are assumed.

ii) Slag layer, molten steel bath: The upper slag surface is modeled as a flat surface, whereby it is assumed that the slag layer in the lower vessel is located 30 mm below the bottom of the slag door, in order to accommodate the definition of a volumetric CO source within the simulation model. The surfaces in contact with the furnace atmosphere are defined to be thermally coupled non-slip walls with a roughness height of 5 mm and an emissivity of 1. A slag layer height of 170 mm is assumed. Therefore the surface of the bath, which is also modeled to be flat, is located 200 mm below the bottom of the slag door. The molten metal layer and foamy slag layer on the bath are modeled as solids, whereby they are defined to have a thermal conductivity of 80 W/(m K) and 8.8 W/(m K) respectively.

The inclusion of the slag layer and a 400 mm thick upper melt layer as solids has the purpose of achieving a qualitatively realistic temperature distribution on the upper surface boundary to the freeboard atmosphere. This results in dependence of the simulated convection and heat radiation exchange at the upper surface and heat conduction down through the slag and molten metal layer. The validity of using this method is discussed in more detail in the results section. The effective thermal conductivity of these two regions was estimated and adapted in dependence of the resulting maximum slag layer temperature. The bottom surface of the molten metal layer is defined to have a constant temperature of 1823 K. By comparison, Guo et al. [3] assume steel bath temperatures in the range of 1773 K to 1873 K.

iii) Gas phase: A total mass flow rate of 3 kg/s of ingress air into the freeboard and a mass flow rate of 7.65 kg/s of air flowing in at the post-combustion gap are defined. The ingress air into the freeboard enters the vessel through the slag door, roof gap and electrode gaps. It is assumed that this mass flow rate is distributed amongst these inlets in proportion to the size of the inlet areas. It is assumed that 0.5 kg/s of steam enters the flow field at the electrode gaps due to the water spray cooling of the electrodes. The current EAF model represents the flat-bath power-on stage of a heat, when coal and oxygen are being blown into the bath using lances. The total mass flow rate of oxygen into the melt during this phase of the heat of the exemplary industrial EAF is 4.28 kg/s. Similarly to the method chosen by Al-Harbi et al. [8], the decarburization of the melt is simulated by a source of CO at the slag surface. It is assumed, simplifying in comparison to Al-Harbi et al., that the oxygen injected into the bath is completely converted into CO. Therefore a homogenous source of CO with a temperature of 1823 K is defined at the slag layer surface. In addition the CO due to electrode consumption is approximated by a homogenous CO source at the electrode surfaces. A corresponding sink for oxygen is also defined by assuming that for every mole of CO entering the flow field, half a mole of O_2 in the gas flowing past the electrode surfaces is used up. The inflows into the solution domain as well as the carbon monoxide sources of the current EAF Model are summarized in **Table 2**.

Table 2: In- and outflows, carbon monoxide sources of the EAF Model

Air ingress (23.4 wt.% O_2, 76.0 wt.% N_2, 0.6 wt.% H_20)		
Slag door	1.51 kg/s	298 K
Roof gap	1.07 kg/s	298 K
Electrode gaps	0.42 kg/s	298 K
Combustion gap	7.65 kg/s	298 K
Steam inflow due to electrode cooling		
Through electrode gaps (directly next to electrodes)	0.5 kg/s	373 K
CO sources and O_2 sink		
Electrode surfaces	0.19 kg/s CO (-0.11 kg/s O_2)	Local gas temperature
Slag surface	7.5 kg/s	1823 K

The static pressures at the in- and outlets are defined relative to an absolute static pressure of 101.325 kPa. A relative static pressure of 0 Pa is defined at the slag door, roof gap, electrode gaps and combustion gap and a turbulent intensity of 5 % is assumed. At the outflow out of the exhaust duct an average relative static pressure of $p_e = -350\ Pa$ is defined. This means that the pressure p_f at the outlet face of each fluid volume adjacent to the outlet area is calculated using equation 14. In this case p_f is a function of the interior cell pressure at the neighboring exit-face p_c and dp, which is the difference in pressure value between p_e and the latest calculated average pressure for the boundary [15].

$$p_f = 0.5\,(p_c + p_e) + dp \qquad (14)$$

iv) Electric arc region: The region around the foot of the arcs, the impingement zone, is assumed to have a truncated cone shape as shown in **Figure 2**.

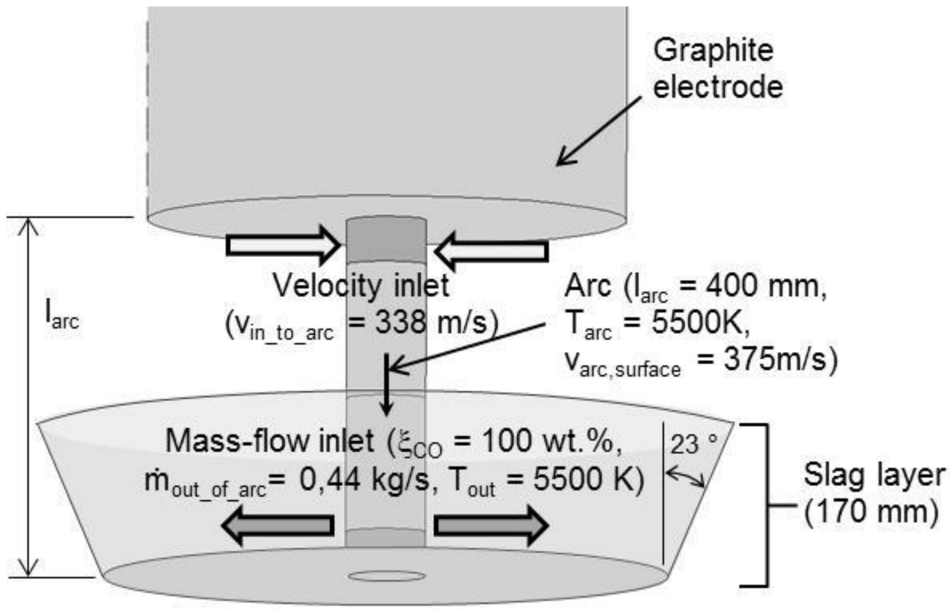

Figure 2: Electric arc region geometry of the EAF Model

A negative velocity inlet is defined at the top of the arc column. Here fluid is drawn out of the solution domain, representing the inflow into each arc, with a velocity of 338 m/s which corresponds to the mass flow rate of 0.44 kg/s calculated by the arc model. When compared to the radial velocities of up to around 400 m/s determined by Quian et al. [14] for the inflow into a 36 kA, 300 mm long DC arc, 338 m/s is acceptable.

At the base of each arc a corresponding mass-flow inlet is defined, where 0.44 kg/s of CO with a temperature of 5500 K flows into the solution domain. The outflow temperature out of the arcs is assumed to be equal to that of the time averaged thermal radiation temperature of the AC arc channels. It was decided to set the mass fraction of CO (Y_{CO}) to 1 at the mass flow inlet because the mass fraction of CO in the fluid around the base of the electrodes is high due to the carbon monoxide source defined at the slag surface.

A constant surface temperature of 5500 K is defined at the surface of the arc cylinders. This temperature for the cylindrical arc surface was estimated to simulate the time averaged thermal radiation temperature of the AC arc channels. It was varied during the development of the model, to determine its influence on the resulting hot spot temperatures at the furnace vessel wall.

With their detailed magneto- fluid dynamic model of a 44 kA DC arc with a length of 300 mm in an air atmosphere Ramírez-Argáez et al. [21] simulate arc temperatures of between 5200 K and 13000 K at the corresponding arc channel radius of the DC arc of 45 mm (CAM). These values were used by Pfeifer et al. [11] for the predecessor version of the EAF model presented in this paper to define a time averaged temperature profile on the cylindrical surfaces representing the AC arcs. In contrast to a steadily burning DC arc, the current flowing in the three AC arc fluctuates as a function of the AC frequency of 50 Hz. Therefore, in order to estimate the time averaged arc temperature, a temperature profile with temperatures of between 9882 K and 3953 K was applied [11], by assuming that the three AC arcs would results in thermal radiation comparable to that of a steady DC arc of similar length and intensity. This temperature profile corresponds to an average temperature of the arc channel surfaces of 7538 K. As this temperature lead to unacceptably high temperatures at the vessel walls when implemented in the EAF model presented in this paper, it was decreased to 5500 K.

In order to include the effect of the arc velocity down towards the bath, the surface of the cylinders are defined as a moving non-slip wall with a roughness height of 5 mm and have a velocity of 375 m/s as shown in Figure 2. The velocity inlet area and mass flow inlet area are defined to have a black-body temperature of 5500 K. Therefore the entire arc length (l_{arc}) of 400 mm gives off intense thermal radiation corresponding to 5500 K. The attachment area of the plasma to the electrodes is defined to have a constant temperature of 3600 K and the contact area between arc and bath is defined to be adiabatic.

v) <u>Electrodes:</u> The electrode surfaces are defined to be thermally coupled non-slip walls with a roughness height of 5 mm and an emissivity of 1.

3.3 Discretization

A mesh sensitivity study was done to check the accuracy and convergence of the results in dependence of the spatial discretization. The meshing was carried out using the software ANSYS Workbench 14.5. The geometry (Figure 1) is divided into 202 volumes. The volumes were meshed step by step in order to ensure that the discretization of the most important regions is fine enough. The meshing is structured in order to minimize the number of cells. Wherever possible the volumes were meshed using the sweep method, with the element size and number of elements on the edges being adjusted in order to ensure that the cell layer at all surfaces corresponds to the wall functions chosen. There is only one solution domain. The solid regions, foamy slag layer and bath layer, are thermally coupled to the fluid regions at the respective boundary. Three simulations (mesh 1 $\approx 0.9 \times 10^6$ cells, mesh 2 $\approx 2 \times 10^6$ cells and mesh 3 $\approx 4 \times 10^6$ cells) with identical boundary conditions were carried out. A mass balance to check the conservation of the elements of the off-gas species (N, O, C and H) was done. In addition, the difference between the simulated energy in- and outflows ($\Delta\dot{E}_{in\text{-}out}$), which for the steady state should be equal to zero, was evaluated. Furthermore the sum of the heat of reaction ($\Delta\dot{E}_{chem.\ Reac.}$) for the solution domain was monitored during each simulation. The convergence of this value was then evaluated by calculating the average difference from the mean value of the heat of reaction in percent for the last 100 iterations.

It was found that the discretization of the chemical species concentration gradients within the flow field is just as important as the mesh quality. All three criteria, namely mass conservation, energy conservation and convergence of the heat of reaction, have to be checked. The results presented in this paper were obtained using mesh 3, which has an average orthogonal quality of 0.96 and an average skewness of 0.10. This mesh is a hybrid mesh which consists to 96 % of hexahedron cells, the rest being tetrahedron, wedge and pyramid cells. Due to the slope of the roof and exhaust elbow geometry, which corresponds to the exemplary geometry of an industrial EAF, it was not possible to completely avoid cells with a low quality. For mesh 3 only 0.05 % of the total number of cells have an orthogonal quality below 0.1. Only 1.0 % of all the cells have a skewness greater than 0.8. However no numerical instability due to these cells, which are mainly located in the roof and elbow, was in evidence. For mesh 3 the maximum error in the mass conservation of the elements of the off-gas species is 0.5 %, $\Delta\dot{E}_{in\text{-}out}$ is equal to 3.2 % and the average difference of the sum of the heat of reaction compared to the mean value of the last 100 numerical iterations was only 0.1 %. In contrast to mesh 1, which had an average difference of the sum of the heat of reaction compared to the mean value of the last 100 numerical iterations of 5.1 %, there was no significant difference between the errors and average difference of the sum of the heat of reaction of mesh 2 and mesh 3. Mesh 3 was chosen due to the better resolution of the gradients within the flow field, which led to a slight difference in the resulting temperature and mass species distributions. Mesh 3, which has approximately 4×10^6 cells and 4×10^6 nodes (3.2×10^6 cells - excluding the post-combustion gap, off-gas extraction, solid slag and bath layer) is very fine in comparison to the discretization of for example of Li et al. [4] (350 000 cells), Chan et al. [5] (82 000 cells) and Sanchez et al [9] (72 604 nodes). Therefore it was decided not to create a fourth mesh with an even finer discretization.

4. Results and Discussion

In order to determine the effect of including the in- and outflow at the arcs on the flow field, two simulations were carried out: Simulation 1 (with the in- / outflow) and Simulation 2 (without the in- and outflow). All other boundary conditions and the mesh are identical. In **Table 3** the resulting energy input of the arc region into the solution domain ($\dot{Q}_{arc\,region}$) for the two simulations is shown. It was calculated with the simulation results using equation (15).

$\dot{E}_{cyl.\,surface}$ is the sum of the simulated net energy input due to thermal radiation exchange of the arcs with the surrounding slag and vessel surfaces and the simulated convection at the cylindrical surface for the assumed time-averaged temperature at the arc channel surface of 5500 K.

$$\dot{Q}_{arc\,region} = \dot{E}_{cyl.\,surface} + \dot{E}_{arc,outflow} - \dot{E}_{arc,inflow} + \dot{Q}_{arc\,/\,electr.} + \dot{Q}_{arc\,/\,melt} \quad (15)$$

Whereby

$$\dot{E}_{arc,inflow} = \dot{m}_{in\_to\_arc} \sum_i^n \left(Y_{i,in\_to\_arc} h_{i,in\_to\_arc}\right) \quad (16)$$

$$\dot{E}_{arc,outflow} = \dot{m}_{out\_of\_arc} \sum_i^n \left(Y_{i,out\_of\_arc} h_{i,out\_of\_arc}\right) \quad (17)$$

For Simulation 1 the fluid drawn in at the top of the arcs has a resulting temperature of 3666 K and the species composition is 98.6 wt. % CO, 1.1 wt. % N_2, 0.1 wt. % CO_2, 0.1 wt. % H_2O and 0.1 wt. % O_2. At the base of the arcs the same mass flow rate (± 0.12 %) with 100 wt. % CO flows out with a temperature of 5500 K. The difference in temperature of the arc in- and outflows of Simulation 1 results in an energy input into the solution domain of 3.26 MW. This represents 17.4 % of the total energy input of the arc region of 18.7 MW. As the contribution by the in- and outflow is not considered in Simulation 2, the contribution due to the net thermal radiation increases to 98.8 %.

Table 3: Energy input of the arc region for simulation 1 and 2

Simulation	**$\dot{Q}_{arc\ region}$**	**$\dot{E}_{cyl.\ surface}$**		**$\dot{E}_{arc,outflow}$ - $\dot{E}_{arc,inflow}$**
		Radiation	**Convection at sides of arc**	
Sim. 1	18.7 MW	82.2 %	0.38 %	17.4 %
Sim. 2	15.7 MW	98.8 %	1.15 %	Without in- and outflow

In **Figure 3** the temperature distributions in the plane through the center of the off-gas duct are shown. For Simulation 1 the temperature range of the fluid in the vortices, resulting from the in- and outflow, is between 3700 and 5000 K. In comparison, the temperature range of the weaker flow vortices in the arc region of Simulation 2, caused by the velocity defined at the surface of the arc cylinders (see Figure 2), is 2500 K to 3000 K. The energy input due to the arc in- and outflows leads to higher temperatures in the freeboard around the electrodes. The normalized vectors shown in Figure 3 indicate that the flow field is also clearly affected.

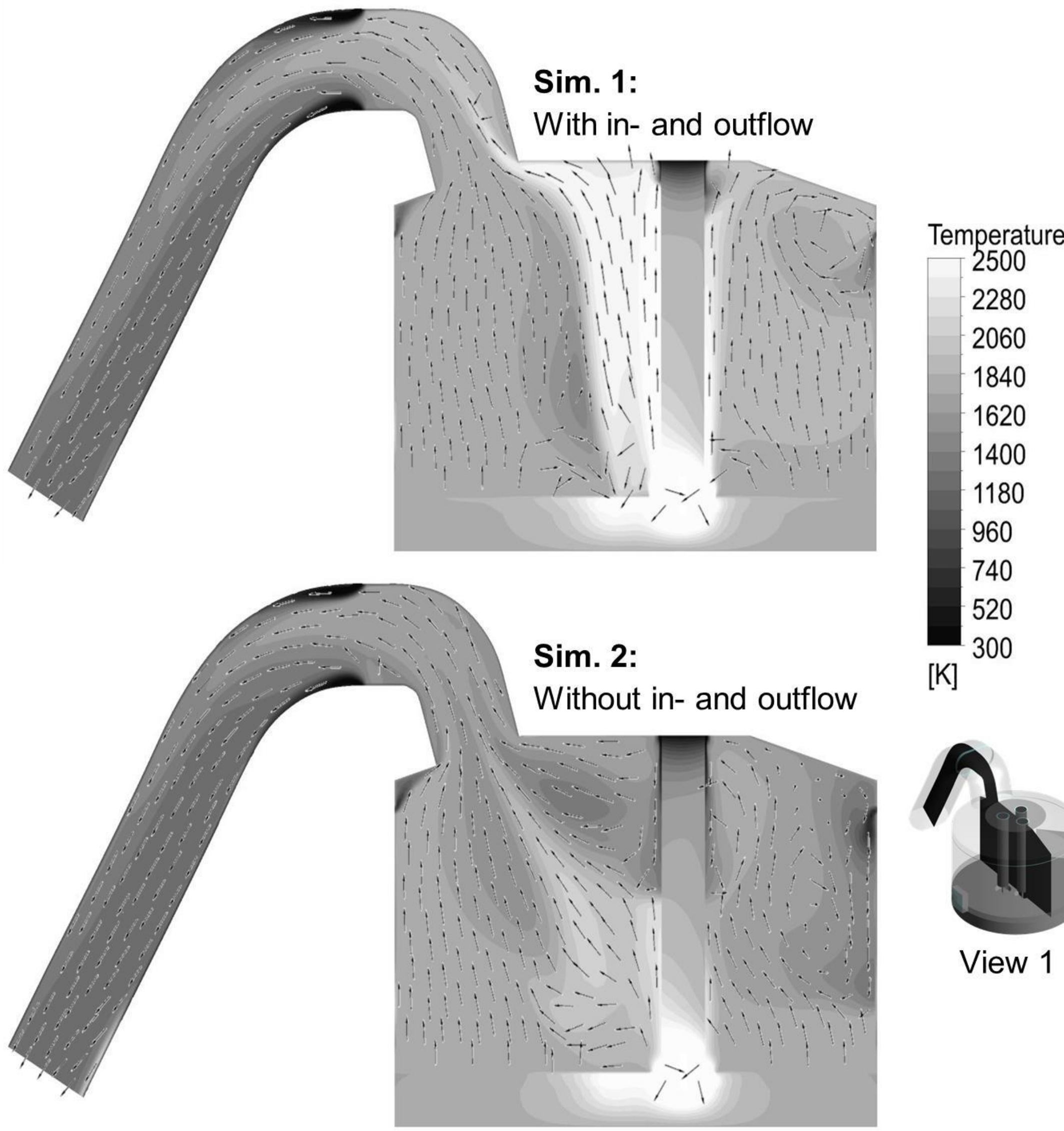

Figure 3: Influence of the arc region on the simulated temperature distribution (View 1)

In **Figure 4** the calculated mass fraction distribution of CO in a plane through the center of two of the electrodes is shown. The normalized vectors and the contours show that there is an increased circulation due to the arc region of Simulation 1, which leads to an increased mixing of the ingress air with CO from the slag surface. Furthermore the accumulation in the balcony area of CO coming out of the slag is reduced. More air from the roof ring gap is drawn down and mixes with the CO.

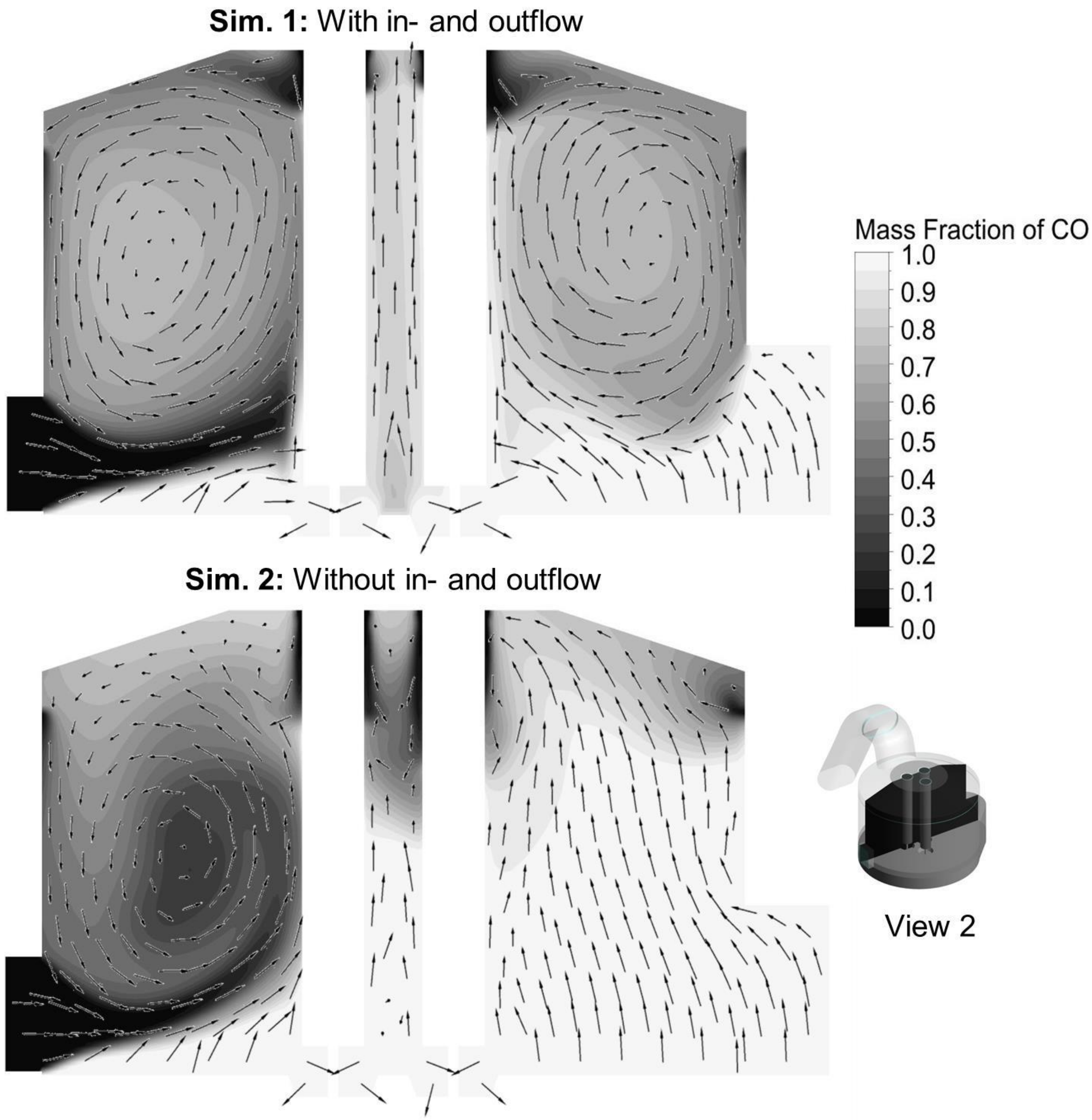

Figure 4: Influence of the arc region on the mass transport of CO from the slag surface (View 2)

The three dimensional nature of the flow within the EAF and the asymmetric effects of slag door inflow, balcony and dedusting over the elbow are evident when comparing Figure 3 and 4. In Figure 3 the contours of Simulation 2 show a core of lower temperatures at the left hand side of the upper vessel below the 4^{th}-hole. This corresponds to the main path of the air from the slag door. For Simulation 1 the increased mixing of air from the slag door with hot CO leads to a less pronounced similar core of lower temperatures, which is located further down, more towards the center of the vessel. This difference in mixing is also evident in Figure 4, where the region of low CO mass fractions to the right and above the slag door, which corresponds to a region with a high mass fraction of O_2 and N_2, is more pronounced for Simulation 2 than for 1.

The results shown in Figure 3 and 4 above correspond to the conditions defined for this particular EAF model. In practice the amount of ingress air will vary and not be evenly distributed with respect to each inflow area. The CO rising up from the slag due to O_2 and carbon injection will not be evenly distributed over the entire slag surface, but will depend on the regions of injection into the melt. These differences and the movement of the AC arcs during each AC cycle will mean that the real 3D flow inside the furnace will be more turbulent. The amount of mixing and the accumulation of CO in the balcony will depend on the position of the O_2 and CO injectors, the amount and distribution of ingress air, and the interaction of the flow of CO from the slag with the arc region and furnace atmosphere.

Equation 18 represents the energy balance equation for the solution domain of the EAF model. The term $\Delta\dot{E}_{chem.reactions}$ refers to the net energy input due to oxidation/dissociation of CO/CO_2. The term $\dot{E}_{sources}$ is the net energy input due to the defined CO sources and O_2 sink. The terms on the left hand side of the equation represent the total energy input, those on the right hand side the total energy output.

$$\dot{Q}_{arc\,region} + \dot{Q}_{Joule\,heating} + \dot{E}_{air} + \Delta\,\dot{E}_{chem.reac.} + \dot{E}_{steam} + \dot{E}_{sources} =$$

$$\dot{Q}_{bath} + \dot{Q}_{cooling} + \dot{Q}_{heat\,loss} + \dot{E}_{off-gas} + \dot{Q}_{conduc.,electrodes} \qquad (18)$$

The increased mixing and the higher temperatures shown by the results of Simulation 1 lead to a corresponding increase in the post-combustion. This is reflected by the higher amount of CO_2 leaving the vessel through the 4th-hole (**Table 4**). The CO_2 mass flow rate out of the EAF freeboard of Simulation 1 is 78 % higher than that of Simulation 2. With the aim of quantifying the simulated increased energy input due to post-combustion within the vessel, a comparison of the total energy input and main outputs for the solution domain up to the 4th-hole is given in Table 4. For Simulation 1, due to the increased post-combustion as well as the increased energy input by the arc region, a total energy input up to the 4th-hole of 36.4 MW results. This is 14.3 % higher than that of Simulation 2.

Table 4: Resulting main energy inputs and outputs

Simulation	$\dot{Q}_{arc\ region}$	$\dot{E}_{Sources,COslag}$	$\dot{E}_{total,in}$	$\dot{Q}_{cooling}$	$\dot{E}_{offgas}$	$\dot{m}_{CO_2,4th\text{-}hole}$
Sim. 1	18.7 MW	13.5 MW	**36.4 MW**	11.6 MW	20.7 MW	0.455 kg/s
Sim. 2	15.7 MW	13.5 MW	**31.9 MW**	10.7 MW	17.9 MW	0.255 kg/s

Guo et al. [3] state that the heat extracted by the cooling water simulated using their radiation model for an arc length of 452 mm varies between 12 and 15 MW. This is comparable to the cooling losses given in Table 4 for an arc length of 400 mm. Furthermore when considering the heat extracted by the cooling water during the refining phase given by Kleimt et al.[20] of approximately 14 MW, calculated using a dynamic energy balance for an exemplary heat of a 140 t industrial DC EAF, these values are in an acceptable range.

The values in Table 4 show that the increased energy input of Simulation 1 is reflected by a corresponding increase in the energy losses due to cooling and the flow of hot off-gas out of the vessel. This is to be expected, as both Sim. 1 and 2 are steady state simulations and therefore do not include the transient heating and absorption processes in the melt. Furthermore, the values show the magnitude of the energy input due to the flow of hot CO out of the slag in relation to the energy input from the arc region, which results from the assumed time averaged thermal radiation temperature of the AC arc channels of 5500 K. In the present model part of the energy absorbed by the bath around the arc region is redistributed within the melt, which is modeled as a solid, and is transported back into the vessel by convection and thermal radiation at the slag surface. This can be seen by the temperature contours in the melt in Figure 3.

Based on these results it is the opinion of the authors of this paper, that in order to correctly simulate the amount of heat absorbed by the melt, the heat transfer due to circulation within the melt away from the surface as well as the heat losses at the refractory/ melt interface would have to be included in the model. In other words the extent of the solution domain should be increased to include the slag and the complete metal phase as liquids.

In **Figure 5** the calculated temperature distribution on the electrodes and slag surface are shown for Simulation 1. The higher temperatures on the slag surface in the balcony region are caused by the simplifying assumption of a homogeneous source of hot CO at the surface of the slag layer. As the balcony walls are defined to be made of refractory material, less heat is drawn out of the vessel here than by the cooling panels, which leads to the non-realistic formation of a hot spot in this area.

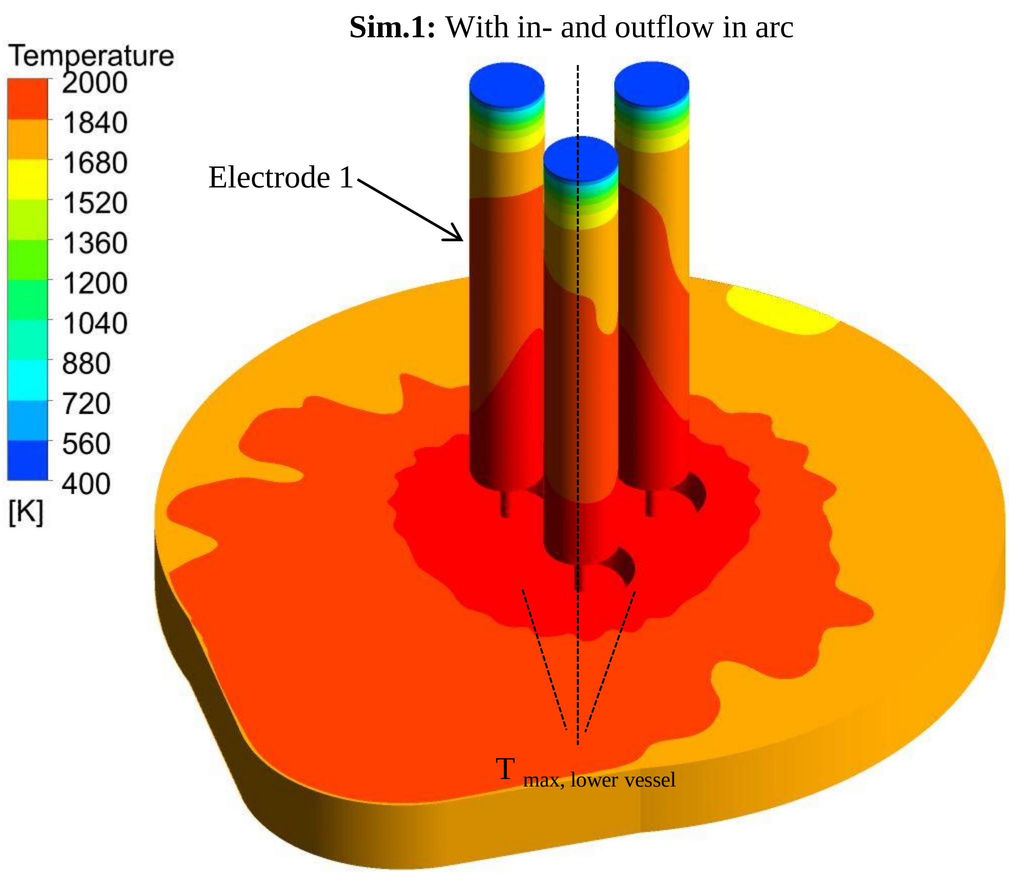

Figure 5: Temperature distribution on the electrodes and slag surface for Sim. 1

The temperature distribution of the electrodes obtained with the numerical EAF model results from the simulated thermal radiation exchange with the arcs, the heat source due to Joule heating within the electrodes, thermal radiation exchange with all other surfaces in the furnace, thermal conduction along the electrode length and convective heat transfer at the electrode surfaces. In **Figure 6** the resulting temperature versus length on the inner and outer side of the electrode furthest away from the 4th-hole, electrode 1, is shown, The simulated temperatures show that the maximum temperature difference between the side facing the other electrodes and the side facing towards the EAF vessel wall of 402 K occurs relatively close to the electrode tip. This temperature difference is approximately 15% of the average electrode temperature at that distance from the tip.

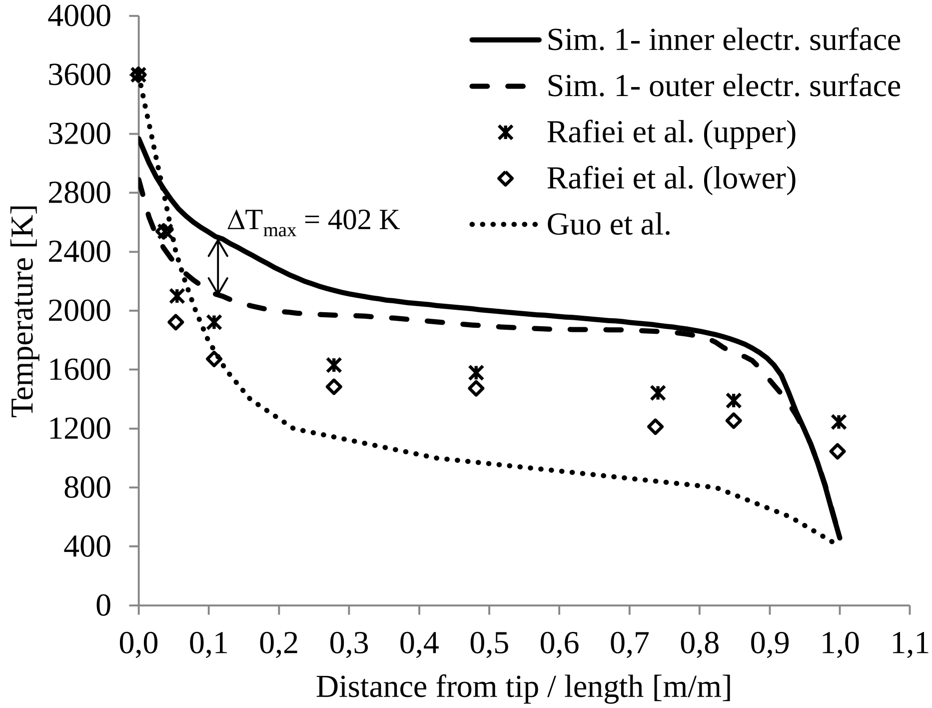

Figure 6: Comparison of electrode temperature profiles

In Figure 6 the simulated temperature profile is also compared to that measured with an infrared pyrometer by Rafiei et al. [22] and to that calculated by Guo et al. [3] (d_{elec} = 610 mm, $T_{elec,tip}$ = 3600 K, $T_{elec,top}$ = 400 K, $T_{furnace}$ = 400 K). Due to the difference in electrode length from the electrode tip to the top of the EAF vessel, which is 3.424 m for the EAF model, 5.400 m for the electrodes considered by Rafiei et al. and 4 m for the electrodes considered by Guo et al. the values are plotted with respect to the distance from the tip divided by the respective electrode length. The measurements by Rafiei et al. [22] were done for electrodes with a diameter of 0.6 m during normal operation of an AC EAF for an alternating electric current of 64 kA [22]. The curves in Figure 6 show, that in comparison to the measurements the assumed temperature of 400 K at the top of the electrode by Guo et al. and used for the EAF model is too low. It leads to a sharp drop in temperature towards the top of the electrode which is not reflected by the measurements. The temperatures resulting with the EAF model agree better to those measured than those of Guo et al. This is due to the assumed furnace atmosphere of 400 K used by Guo et al. Even though the slope of the central part of the simulated profile obtained using the EAF model is similar to that measured, the temperatures are higher. Unfortunately, Rafiei et al. do not clearly describe how and when the temperature measurements were done, only stating that they were done at a distance of approximately 5m from the electrodes. In order to be able to measure the temperature profile of the entire electrode length, it's most likely that this was done during charging, so that the temperatures would tend to be rapidly dropping during the measurement. The difference between the measured and simulated profile at the electrode tip is a consequence of the simplified electrode geometry. In conclusion, the electrode temperature profile simulated using the EAF model shows that the thermal radiation exchange between the electrodes leads to a difference in temperature at the respective height that is not negligible. For future versions of the model the electrode top temperature should be reconsidered and the shape of the electrodes at the tip adapted.

When assuming a fixed temperature profile on the electrodes, the distribution of the energy input coming from the arcs is not calculated correctly. The fraction of this energy absorbed and redistributed along the electrodes length is then not included in the simulation properly. In order to be able to compare the calculated energy flows to the electrical energy input, the electrodes have to be part of the solution domain.

In **Figure 7** the temperature distribution on the vessel walls is shown. The reason for the pattern of the hot spot formation can be explained by considering their position with respect to the thermal radiation from the arcs as illustrated in Figure 5. The hot spots form as a function of the sum of the radiation exchange with the inner surfaces in dependence of the respective line of sight and the amount of radiation absorbed by the gas between the surfaces.

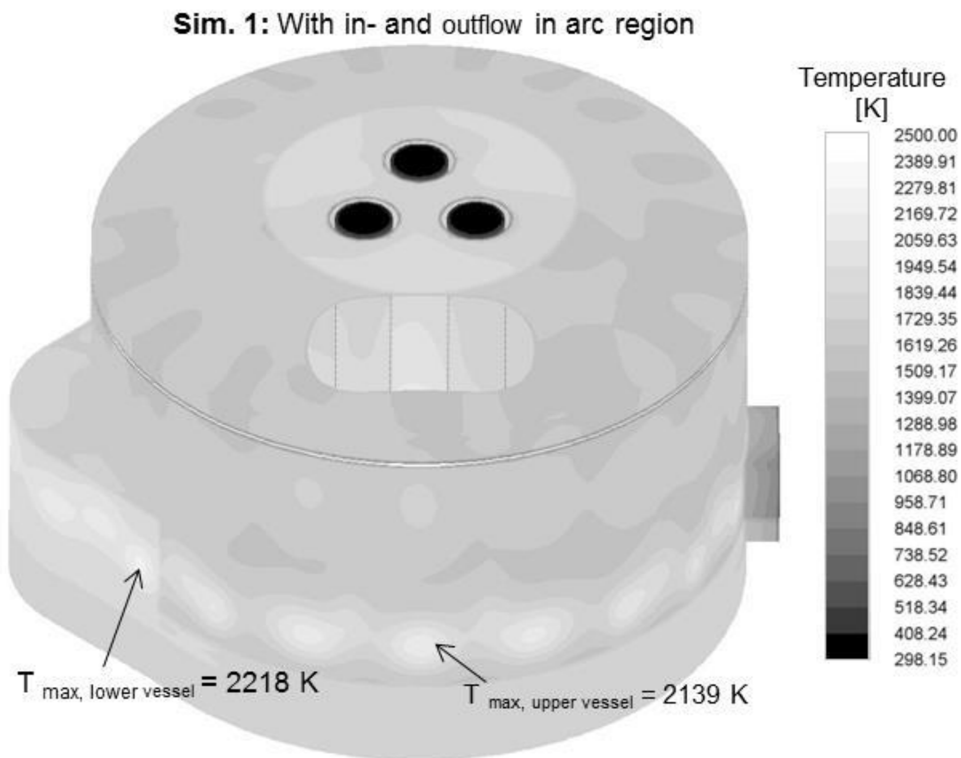

Figure 7: Temperature distribution on the EAF walls for Sim. 1

The maximum simulated hot spot temperature of the water cooled upper vessel is 2139 K. At this temperature the slag layer protecting the water cooled panels of the vessel would melt and damages to the panels are to be expected as the maximum allowable temperature to avoid perforation of the panels is in the order of 1800 K [9]. Taking into account, that the slag height simulated is only about 43 % of the arc length and that the arcs therefore are simulated as relatively free burning arcs this result is still realistic even if not desirable in EAF operation.

The implementation of further energy sources and sinks, for example to represent the transient heating of the melt, needs to be further investigated. These phenomena need to be included in the model e.g. as energy sinks in slag and metal or, alternatively, quantified in order to be able to compare the true energy input of the secondary circuit to that being transferred by the arc region in the model. Then the correct time averaged temperature of the arcs needed for the model could be found. These findings correspond to those of Henning et al. [7], who use a process energy absorption model to take the energy absorbed in the slag and bath layer into account. For the simulations presented by Henning et al. for steady state heat loss conditions an operating power of 6 MW is defined. In comparison, when considering the process energy absorbed in the slag and bath region, an operating power of 46 MW is defined.

5. Conclusions

Even though there are still many aspects of the model that need to be further developed, it can be used to investigate the influence of individual operation parameters, for example the slag height or the amount or location of air ingress, on the post-combustion or thermal loading of the cooling panels. The present model, combining the simulation of the arc region and the simulation of the electrodes within the complete freeboard of an industrial EAF with its asymmetric geometry, is a useful tool to understand the three-dimensional nature of the heat and mass transport within the EAF vessel.

Main findings based on the presented results are:

i) The effect of the in- and outflow into the arc region should not be neglected, as it represents one of the relevant energy input mechanisms of the arc region and leads to an increased mixing and post-combustion of the gas species within the furnace.

ii) When considering the energy flows within the current EAF model it becomes evident that it is essential to include the graphite electrodes in order to be able to model the redistribution of the energy within the furnace correctly.

iii) In order to achieve the long term goal of being able to compare the real electric energy input to the modeled energy flows, the individual energy sources and sinks within the arc region and in the bath, need to be further investigated and added to the model. Therefore it is recommended that for future models the flow within the slag layer and metal bath be included in the solution domain.

6. Nomenclature

$\Delta\dot{E}_{\text{in-out}}$	: Difference between energy in- and outflows of the solution domain
$\Delta\ \dot{E}_{\text{chem. Reac.}}$	: Net energy input due to oxidation/dissociation of CO/CO_2
$\vec{g}$	: Gravity vector
S_m	: Represents mass sources within the solution domain
Y_i	: Local mass fraction of species i
$\vec{F}$	: Represents external body forces and momentum sources
S_h	: Volumetric heat sources within the flow field
k	: Turbulent kinetic energy
ε	: Dissipation rate
μ_t	: Turbulent viscosity
ρ	: Density
$\vec{v}$	: Velocity vector
p	: Static pressure
τ	: Stress tensor
E	: Internal energy of gas atmosphere
k_{eff}	: Effective thermal conductivity
$\overline{\overline{\tau}_{eff}}$	: Effective shear stress tensor
T	: Static temperature
h_i	: Sensible enthalpy of species i

h_j	: Sensible enthalpy of species *j*
$\vec{J_j}$	: The diffusion flux of species *j*
s	: Path length
$\vec{s}$	: Direction vector
$\vec{r}$	: Position vector
a	: Absorption coefficient
I_{rad}	: Incoming thermal radiation intensity
σ_s	: Scattering coefficient
n	: Refractive index
σ	: Stefan-Boltzmann constant
Φ	: Phase function
Ω'	: Solid angle
$k_{f,r}$	: Forward rate constant for reaction r
A_r	: Pre-exponential factor for reaction r
β_r	: Temperature exponent for reaction r
E_r	: Activation energy for reaction r
R	: Universal gas constant
$\hat{R}_{i,r}$	: Molar rate of creation or destruction of species i
$C_{j,r}$	: Molar concentration of species *j* for reaction *r*
$\eta'_{j,r}$	: Rate exponent for reactant species *j* in reaction *r*
$\eta''_{j,r}$	: Rate exponent for product species *j* in reaction *r*
$\dot{q}'''$	: Specific heat flow
I_{elec}	: Effective electric current

R_{elec}	: Electrical resistance
$V_{electrode}$	: Volume of the graphite electrodes
$j_{arc, CAM}$	: Mean electric arc current density
r_{arc}	: Electric arc radius (CAM)
$\dot{m}_{arc,CAM}$	: Mass flow rate through a stationary electric arc (CAM)
μ_0	: Magnetic field constant
$\dot{Q}_{arc\ region}$	: Energy input from arc region
$\dot{E}_{arc,inflow}$	: Energy <u>out</u>flow out of solution domain due to inflow into arc columns
$\dot{E}_{arc,outflow}$	: Energy <u>in</u>put due to flow into solution domain at the base of each arc
$\dot{E}_{cyl.\ surface}$	: Net energy input due to thermal radiation and convection at the cylindrical surface
$\dot{Q}_{arc\ /\ electr.}$	: Energy input at plasma / electrode interface
$\dot{Q}_{arc\ /\ melt}$	: Energy input at plasma / melt interface
$\dot{Q}_{Joule\ heating}$	: Energy input due to Joule heating of the electrodes
$\dot{E}_{air}$	: Energy input due to inflow of air
$\dot{E}_{steam}$	: Energy input due to inflow of steam from electrode cooling
$\dot{E}_{sources}$	: Energy input due to CO sources and energy loss due to O_2 sink
$\dot{Q}_{bath}$	: Net energy flow at bottom surface
$\dot{Q}_{Cooling}$	: Energy outflow due to cooling
$\dot{Q}_{Heat\ loss}$	: Energy outflow due to heat losses at the walls without cooling panels
$\dot{E}_{off\text{-}gas}$	: Energy loss due to outflow of off-gas
$\dot{Q}_{conduc.electrodes}$	: Energy outflow by conduction at top surface of electrodes

d_{elec} : Electrode diameter

$T_{elec,tip}$: Electrode tip temperature

$T_{elec,top}$: Electrode top temperature

$T_{furnace}$: Assumed homogeneous furnace atmosphere temperature

References

[1] M. Kirschen, H. Pfeifer, F. J. Wahlers, *Proc. of 7'th European Electric Steelmaking Conference*, European Coal and Steelmaking Community, Venice, **2002**, p. 2.3.

[2] V. Logar, D. Dovžan, I. Ŝkrjanc, *ISIJ Int.* **2012**, 52, p. 413.

[3] D. Guo, G.A. Irons, *Proc. of AISTech* **2004**, Volume 1, AIST, Warrendale, p. 991.

[4] Y. Li, R. J. Fruehan, *Metall. Mater. Trans. B* **2003**, 34B, p. 333.

[5] E. Chan, M. Riley, M. J. Thomson and E.J. Evenson: *ISIJ Int.* **2004**, 44, p. 429.

[6] B. Henning, M. Shapiro, L. A. le Grange, *Proc. of 10th International Ferroalloys Congress*, SAIMM **2004**, Johannesburg, p. 565.

[7] B. Henning, M. Shapiro, L. A. le Grange, *Proc. of 11th International Ferroalloys Congress, SAIMM* **2007**, Johannesburg, 654.

[8] M. N. Al-Harbi, S. K. Mishra, M. Maity, S. Al-Turky, *Proc. of METEC InSteelCon* **2011**, Stahlinstitut VDEh, Düsseldorf, p. 1

[9] J. Sanchez, A. Conejo, M. Ramirez-Argáez, *ISIJ Int.* **2012**, 52, p. 804.

[10] J. Sanchez, M. Ramirez-Argáez, A. Conejo, *Steel Research Int. 80,* **2009**, 2, p. 113.

[11] H. Pfeifer, T. Echterhof, L. Voj, J. Gruber, H.-P. Jung, S. Lenz, C. Beiler, F. Cirilli, U. De Miranda, N. Veneri, E. Bressan, *EUR 25078 - Control of nitrogen oxide emission at the electric arc furnace – CONOX* **2012**, European Commission, Luxembourg, p. 92.

[12] H. Pfeifer, *Energetische Untersuchung der Plasmatechnik bei der Stahlerzeugung, Stahleisen* **1992**, Düsseldorf, p. 57.

[13] G. R. Jordan, B. Bowman, D. Wakelam, *Electrical and photographic measurements of high-power arcs*, British Steel Corporation, Swindon Laboratories, Moorgate, England, **1970**, p. 1089

[14] F. Qian, B. Farouk, R. Mutharasan, *Metall. Mater. Trans. B* **1995**, 26B, p. 1057.

[15] ANSYS FLUENT Theory Guide **2013**, Release 14.5, ANSYS

[16] G. D. Raithby, E. H. Chui, *J. Heat Transfer* **1990**, 112, p. 415.

[17] T. F. Smith, Z. F. Shen, J. N. Friedman, *J. Heat Transfer* **1982**, 104, p. 602.

[18] T.-H. Shih, W. W. Liou, A. Shabbir, Z. Yang, J. Zhu, *A New Eddy-Viscosity Model for High Reynolds Number Turbulent Flows - Model Development and Validation* **1995**, Computers Fluids. 24(3), p. 227.

[19] B. E. Launder, D. B. Spalding, *The Numerical Computation of Turbulent Flows* **1974**, Computer Methods in Applied Mechanics and Engineering. 3, p. 269.

[20] K. J. Thomé-Kozmiensky, D. Goldmann, *Recycling und Rohstoffe*, Band 5, TK Verlag Karl Thomé-Kozmiensky, Neuruppin, (2012), p. 381.

[21] M. A. Ramírez-Argáez, C. González-Rivera, G. Trápaga, ISIJ Int. **2009**, 49, No. 6, p.796

[22] R. Rafiei, A. Kermanpur, F. Ashrafizadeh, Ironmaking and Steelmaking **2008**, 35, Nr. 6, p. 465.